J. Fluid Mech. (1981), *vol.* 111, *pp.* 123–140
Printed in Great Britain

Growth and collapse of a vapour cavity near a free surface

By J. R. BLAKE

Department of Mathematics, University of Wollongong,
Wollongong, New South Wales, Australia

AND D. C. GIBSON

Division of Mechanical Engineering,
Commonwealth Scientific and Industrial Research Organization,
Highett, Victoria, Australia

(Received 6 August 1980 and in revised form 5 February 1981)

An approximate integral-equation approach is used to model the growth and collapse of a vapour cavity in close proximity to an initially plane free surface. By comparison with experiment, it is shown to predict all the salient features of the bubble and free-surface interaction, provided that the complete nonlinear Bernoulli pressure condition is applied on both surfaces. Features observed and predicted include the formation of an accelerating liquid jet in the bubble and a pronounced spike in the free surface during the collapse phase of the bubble's life. If the bubble is initially sufficiently close to the free surface, it will become 'entrained' in the raised free surface with a veneer of liquid separating the two free surfaces.

1. Introduction

The observation of the growth and subsequent collapse of a vapour cavity (or cavitation bubble) dates back almost a century, when Osborne Reynolds (1894) noted their formation in water flowing through constricted tubes. The bubbles arise because of a local lowering of the dynamic pressure below the saturated vapour pressure. This phenomenon is most pronounced near propeller or turbo-machinery blades, where one might expect high-speed fluid motion. A clear illustration of the formation of cavitation bubbles near a ship propeller can be found in Batchelor (1967, plate 16). The collapse of vapour bubbles near propeller blades was found, by a special commission instituted by the British Admiralty in 1915, to be the prime mechanism causing damage to the blades. Rayleigh (1917) considered the growth and collapse of a spherical bubble in an infinite fluid and showed that tremendous dynamic pressures arise during the collapse phase of the bubble's life.

The spherical implosion described by Rayleigh was accepted as the root cause of cavitation damage for almost 50 years, until Benjamin & Ellis (1966) and others recorded the asymmetric collapse of an initially spherical vapour cavity near a rigid boundary. The bubble collapses with a high-speed liquid jet directed towards the boundary. Later studies by Gibson (1968) suggested that the physical properties of the boundary determined the direction of movement of the liquid jet during the collapse phase. For example, in some of his experiments the jet was directed away from a flexible boundary. The Benjamin & Ellis observations were later predicted theoretically by Plesset & Chapman (1971) in their finite-difference solution of the equations

of motion. Their calculations predicted maximum jet velocities between 130 and 180 m/s for physically relevant parameters. These calculations were confirmed experimentally by Lauterborn & Bolle (1975).

Other studies by Shima (1968) and Mitchell & Hammitt (1973), using analytical and numerical approaches respectively, came to similar conclusions to those of Benjamin & Ellis and Plesset & Chapman concerning the asymmetric collapse of a cavitation bubble. An interesting approximate integral-equation approach was used by Bevir & Fielding (1974) to model the early stages of the collapse phase of a cavitation bubble. In their approach they use a distribution of sources and derivatives (e.g. doublets) wholly contained within the bubble and located along the axis of symmetry. This method has the advantage that it requires minimal computational effort in comparison to the much more expensive 'marker and cell' finite-difference approaches of Plesset & Chapman (1971) and Mitchell & Hammitt (1973). Its main disadvantage is that the method fails during the latter stages of jet formation. This is due to the decrease in the centre-line length on which the singularities are distributed, so restricting the resolution of the surface shape. In the analysis presented in this paper (§ 2), a modification of this approach will be used to study the growth and collapse of a bubble near a free surface.

The motivation behind this study stems from the possibility of coating turbomachinery blades with a suitably resilient material so that the jet is directed away from the boundary. From the law of Bjerknes (see, for example, Birkhoff & Zarantonello 1957) concerning the migration of oscillating bubbles near boundaries, it can be shown that oscillating bubbles tend to migrate towards rigid boundaries (e.g. a ship hull, propeller or sea bottom) and away from a free surface. The migratory behaviour near a flexible boundary and the consequential jet motion is not fully understood. For example, Gibson (1968) and Gibson & Blake (1980) record results where the bubble motion and jet are directed away from a flexible boundary.

In a theoretical paper Blake & Cerone (1981) showed that the behaviour of a vapour bubble near an inertial boundary with a prescribed mass per unit area depended on the value of the parameter α defined by

$$\alpha = \rho h/\sigma.$$

Here ρ is the density of the liquid, h the initial distance of the cavitation bubble from the boundary and σ the mass per unit area of the boundary. For $\alpha < 0{\cdot}8$, the bubble exhibited behaviour similar to that observed near a rigid boundary by migrating towards the boundary, while for $\alpha > 0{\cdot}8$ the bubble moved away. At $\alpha = 0{\cdot}8$, the bubble remained almost stationary as if it were located in an infinite fluid. To obtain these results the Bernoulli pressure term on the inertial boundary was linearized, thus restricting the location of the bubble to at least one maximum bubble diameter from the boundary. Clearly for any realistic simulation of the interaction between a vapour bubble and a flexible boundary the nonlinear boundary conditions must be applied. To see the importance of the nonlinear terms in the analysis, we compare the linear and nonlinear theories for the most trivial flexible boundary, a free surface!

Recently Chahine (1977) has carried out a theoretical and experimental study on the growth and collapse of a cavitation bubble near a free surface. He suggests that the use of the linearized boundary condition in this case is only applicable if the bubble

centroid depth h is greater than $2{\cdot}2R_m$, where R_m is the maximum 'radius' of the cavity. The experimental results of Chahine were also particularly interesting. For a cavity a sufficient distance away from the free surface, the free surface grows and collapses with the bubble growth and collapse; much as one might expect from linear theory. However, for the cases in which the bubble centroid depth is approximately equal to R_m, a completely different phenomenon for the free surface was observed. In this case the free surface near the axis of symmetry continues to grow during the collapse of the bubble. Furthermore, during the late growth and early collapse phase of the bubble life the bubble becomes 'entrained' beneath the elevated free surface.

In this paper we develop an approximate integral-equation approach, along the lines of Bevir & Fielding (1974), to model the growth and collapse of a vapour bubble near a free surface. In § 2 comparisons are made between the linear and nonlinear theories. It is clear that the nonlinear Bernoulli pressure term has to be applied on both free surfaces.

As a check on the numerical calculations, conservation of mass, momentum and energy are checked at each time step. In § 3, we describe the experimental rig in which the growth and collapse phases, including the jet and free surface motion, are recorded on a high-speed ciné film. In § 4, the theoretical predictions and experimental observations are compared for several initial centroid positions. Data predicted, recorded and compared include bubble shape and centroid position as a function of time, and bubble lifetime as a function of initial position of the centroid. In the final § 5 the main conclusions of this work are summarized and the possible ramifications of the work are discussed in relation to flexible boundaries which have both mass and rigidity.

2. Theory

As the growth and collapse phases of the vapour bubble and the free-surface plume are symmetric, we shall use a cylindrical polar co-ordinate system omitting the angular dependence. Thus, as is illustrated in figure 1 (a), we specify the shape of the vapour cavity by N_1 points (rings) lying on the bubble surface. The free surface is specified in a like manner; in this case using N_2 points (rings). During the ensuing analysis, we shall trace the movement of these particles through the growth and collapse phases of the bubble life. In the calculations, two alternative distributions of points were used at time $t = 0$, one an equally spaced case and the other a cosine distribution which placed more points near the top and bottom of the bubble and near the axis of symmetry of the free surface. This latter case was found to be more appropriate, providing higher resolution of the bubble and the free surface. In practice we shall be tracing the Lagrangian movement of a fluid particle on the bubble surface and on the free surface.

On the other hand, we will use an Eulerian description for the general fluid motion. To simulate the fluid motion, we shall assume the fluid is incompressible and inviscid. Thus we will be neglecting viscous forces – the Reynolds numbers are $O(10^4)$, so viscous effects will be restricted to a thin boundary layer around the bubble. Surface-tension forces can also be neglected but they may be important, initially when the bubble is small and late in the collapse phase after the jet has formed. Gravitational forces are also neglected because cavitation bubbles are usually small and have a very short life, so that buoyancy effects are small. This is not the case in our experiments,

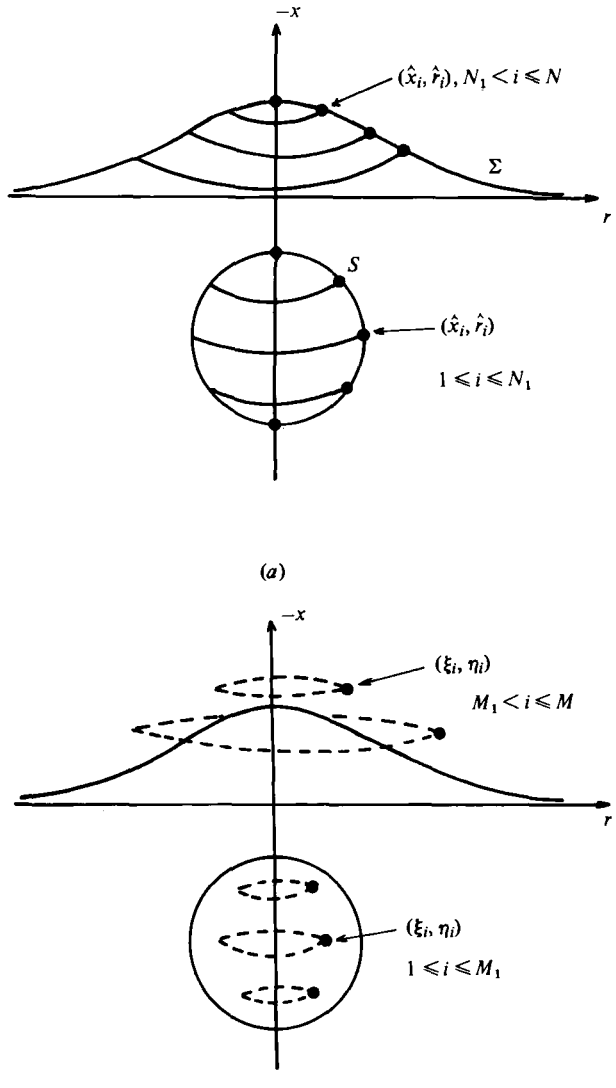

FIGURE 1. (*a*) The surface specification. (*b*) The singularity distribution used in the numerical model of vapour bubble and free surface interaction.

where large, slowly pulsating bubbles are studied and similitude is achieved by conducting the experiments under free-fall conditions.

With these assumptions we may represent the velocity as the gradient of a potential which in turn, because of the incompressibility of the fluid, satisfies Laplace's equation. That is

$$\mathbf{u} = \nabla\phi, \quad \nabla^2\phi = 0, \tag{1}$$

where $\mathbf{u}$ is the Cartesian velocity vector and ϕ is the potential. The conditions at infinity are

$$\mathbf{u} \to 0 \quad \text{and} \quad p \to p_\infty, \tag{2}$$

where p is the pressure and p_∞ is the constant pressure at infinity and on the free surface. The kinematic and dynamic boundary conditions on the cavity surface are

$$\mathbf{u}_s = \mathbf{u} \quad \text{and} \quad p = p_c, \tag{3}$$

where $\mathbf{u}_s$ is the velocity of a particle on the surface and p_c is the assumed constant saturated vapour pressure in the cavity. Applying the Bernoulli condition we obtain

$$p_c = p_\infty - \rho \frac{\partial \phi}{\partial t} - \tfrac{1}{2}\rho \mathbf{u}^2, \tag{4}$$

where ρ is the fluid density.

On the free surface, we shall use one of two conditions, depending on whether we use the linear or nonlinear dynamic boundary condition. In the linear case, the integrated form of the boundary condition yields

$$\phi = 0 \quad \text{on} \quad x = 0. \tag{5a}$$

In the nonlinear case, we equate the Bernoulli pressure to the pressure at infinity (i.e. on the free surface), in

$$\frac{\partial \phi}{\partial t} + \tfrac{1}{2}\mathbf{u}^2 = 0 \quad \text{on} \quad x = \zeta(r, t), \tag{5b}$$

where $\zeta(r, t)$ is the location of the free surface with positive values being into the fluid. The kinematic condition on the free surface in an Eulerian description is the usual

$$\frac{D(\zeta - x)}{Dt} = \left(\frac{\partial}{\partial t} + \mathbf{u} \cdot \nabla\right)(\zeta - x) = 0. \tag{6}$$

In the Lagrangian description the velocity of a fluid particle on the free surface is taken as the free-surface velocity.

The initial conditions on the free surface are that $\zeta = 0$ and $\phi = 0$ while on the cavity we use a small sphere of radius R_0 with a potential derived previously in Gibson & Blake (1980) and given by the formula

$$\phi_0 = -R_0 \left[\frac{2}{3}\left(\frac{p_\infty - p_c}{\rho}\right)\left\{\left(\frac{R_m}{R_0}\right)^3 - 1\right\}\right]^{\frac{1}{2}}. \tag{7}$$

Here R_m is the maximum bubble size which is controlled by p_∞, p_c and the initial kinetic energy of the fluid. This is exactly the potential one would obtain for a cavity in an infinite fluid. This is a justifiable approximation in that, at $t = 0$, the position of the bubble centroid h is taken to be much greater than the initial radius R_0. Both the linear and nonlinear problems are now well-posed; the approximate method of solution will now be described.

We derive the time-dependent solution via an approximate integral-equation approach similar to that suggested by Bevir & Fielding (1974). The approach used was a line distribution of appropriate singularities along the axis wholly inside the cavity. In the problem discussed in this paper, we find that discrete ring distributions of singularities are physically more appropriate than the line distribution approach and we can choose the distribution such that the mass flux (i.e. essentially the source strength) through the frustrum adjacent to the ring source is approximately constant and hence computationally desirable.

Thus we define the potential as the sum of a finite number of ring sources as follows:

$$\phi(x,r) = \sum_{i=1}^{M=M_1+M_2} m_i(\xi_i,\eta_i)\, G(x,r;\xi_i,\eta_i), \tag{8}$$

where

$$G(x,r;\xi_i,\eta_i) = -\eta_i K(k)/\pi r_2, \quad k^2 = 1-r_1^2/r_2^2, \tag{9a,b}$$

$$r_1^2 = (x-\xi_i)^2+(r-\eta_i)^2, \quad r_2^2 = (x-\xi_i)^2+(r+\eta_i)^2, \tag{9c,d}$$

and where (ξ_i,η_i) are located on a surface S' inside the bubble surface S ($1 \leqslant i \leqslant M_1$) or on Σ', a surface exterior to the free surface Σ ($M_1 < i \leqslant M$). In the calculations, the points on the surface S were usually taken at the half radius while the points on Σ' are $0{\cdot}25R_m$ above the free surface. Here $K(k)$ is a complete elliptic integral of the first kind (Abramowitz & Stegun 1965). For the linearized free-surface example we can omit the distribution over Σ' and use the Green's function that identically satisfies the boundary condition (5a) as follows:

$$G_L(x,r;\xi,\eta) = G(x,r,\xi,\eta)-G(x,r;-\xi,\eta). \tag{10}$$

Initially, and at each successive time step, we know, or can calculate, the potential ϕ_j at each 'marked' point (x_j,r_j) $(j = 1, N = N_1+N_2)$ on the vapour cavity and on the free surface. By substitution of these values into (8), we obtain the following set of linear equations for the unknown source distributions m_i $(i = 1, M)$

$$\phi_j = A_{ji} m_i, \quad i = 1, M \quad \text{and} \quad j = 1, N, \tag{11a}$$

where

$$A_{ji} = G(x_j,r_j;\xi_i,\eta_i). \tag{11b}$$

If $M = N$ in (11a), we may solve for m_i via collocation; however, more commonly a least-squares approach was used to derive m_i. In this latter case, we often used $M_1 = M_2 = 11$ and $N_1 = 31$ and $N_2 = 21$, which had the advantage of smoothing the potential distribution on both the vapour cavity and the free surface. With knowledge of the source distribution, we may now calculate the particle velocities as follows,

$$u_j = \left[\frac{\partial\phi}{\partial x}\right]_{(x_j,r_j)} = \sum_{i=1}^{M} m_i \left[\frac{\partial G}{\partial x}\right]_{(x_j,r_j)}, \tag{12a}$$

and

$$v_j = \left[\frac{\partial\phi}{\partial r}\right]_{(x_j,r_j)} = \sum_{i=1}^{M} m_i \left[\frac{\partial G}{\partial r}\right]_{(x_j,r_j)}. \tag{12b}$$

Immediately, we can use a simple Euler scheme to calculate the next position of the particle, a time Δt later,

$$x_j(t+\Delta t) = x_j(t)+u_j(t)\,\Delta t+O(\Delta t^2), \quad r_j(t+\Delta t) = r_j(t)+v_j(t)\,\Delta t+O(\Delta t^2), \tag{13a,b}$$

where $j = 1, N$. The potential ϕ is a function of both position and time, and therefore, in updating the potential, we need to use the material derivative

$$\begin{aligned}\phi_j(t+\Delta t) &= \phi_j(t)+\left[\frac{D\phi}{Dt}\right]\Delta t+O(\Delta t^2)\\ &= \phi_j(t)+\left[\frac{\partial\phi}{\partial t}+u^2\right]\Delta t+O(\Delta t^2).\end{aligned} \tag{14}$$

Conveniently the Bernoulli pressure conditions on the vapour cavity (4) and the free surface (5*b*) can be used to eliminate the $\partial\phi/\partial t$ term as follows.

On the vapour cavity we obtain

$$\phi_j(t+\Delta t) = \phi_j(t) + \left[\frac{p_\infty - p_c}{\rho} + \tfrac{1}{2}\mathbf{u}^2\right]\Delta t + O(\Delta t^2), \quad 1 \leqslant j \leqslant N_1, \tag{15a}$$

while on the free surface

$$\phi_j(t+\Delta t) = \phi_j(t) + \tfrac{1}{2}\mathbf{u}^2\Delta t + O(\Delta t^2), \quad N_1 \leqslant j \leqslant N. \tag{15b}$$

The time increment Δt is carefully chosen so that the potential can only change by at most a specified fixed amount of $\Delta\phi$. Thus by using (13*a*, *b*) we can update the boundary shape while (15*a*, *b*). are used to update the surface potentials. The approximate method of solution described above was used to simulate the growth and collapse phases of the bubble.

At each time step conservation of mass, momentum and energy were checked to see that the variation was within specified bounds (usually less than $\pm 2\,\%$). Conservation of mass yields the following integral and algebraic relations:

$$\int_S \frac{\partial\phi}{\partial n}\,dS = 2\pi \sum_{i=1}^{M_1} \eta_i m_i. \tag{16}$$

Conservation of momentum, after appropriate rearrangement and integration, yields a Kelvin-impulse-type term **I** defined as follows (Wu 1976; Blake & Cerone 1981)

$$\mathbf{I} = \mathbf{I}_0 = \int_S \phi\mathbf{n}\,dS = \int_0^t \mathbf{F}_e(t)\,dt, \tag{17}$$

where

$$\mathbf{F}_e(t) = \rho\int_{\Sigma_b}\left\{\tfrac{1}{2}(\nabla\phi)^2\,\mathbf{n} - \frac{\partial\phi}{\partial n}\nabla\phi\right\}dS = \frac{d\mathbf{I}_1}{dt} \tag{18}$$

Blake & Cerone (1981) showed that, for the linearized free-surface example, the x-component of $\mathbf{F}_e$ was greater than zero for all time, in other words I_x is a non-decreasing vector function of time, directed away from the free surface (with x positive into the liquid).

The sum of the total kinetic and potential energies must be a constant E_0 for all time:

$$E = \overline{T} + v = E_0. \tag{19}$$

The kinetic energy $\overline{T}$ can be evaluated in terms of the following integrals over the bubble and free surface,

$$\overline{T} = -\tfrac{1}{2}\rho\left[\int_S + \int_{\Sigma_b}\right]\phi\frac{\partial\phi}{\partial n}\,dS. \tag{20}$$

The potential energy v is equal to the volume V of the bubble multiplied by the pressure difference $(p_\infty - p_c)$, i.e.

$$v = (p_\infty - p_c)\,V. \tag{21}$$

Maximum bubble radius is defined in terms of the maximum volume of the spherical vapour cavity in an infinite fluid. In this case all the kinetic energy is converted into potential energy. However, when flexible boundaries are present, considerable kinetic energy may remain in the fluid even when the bubble has reached maximum size.

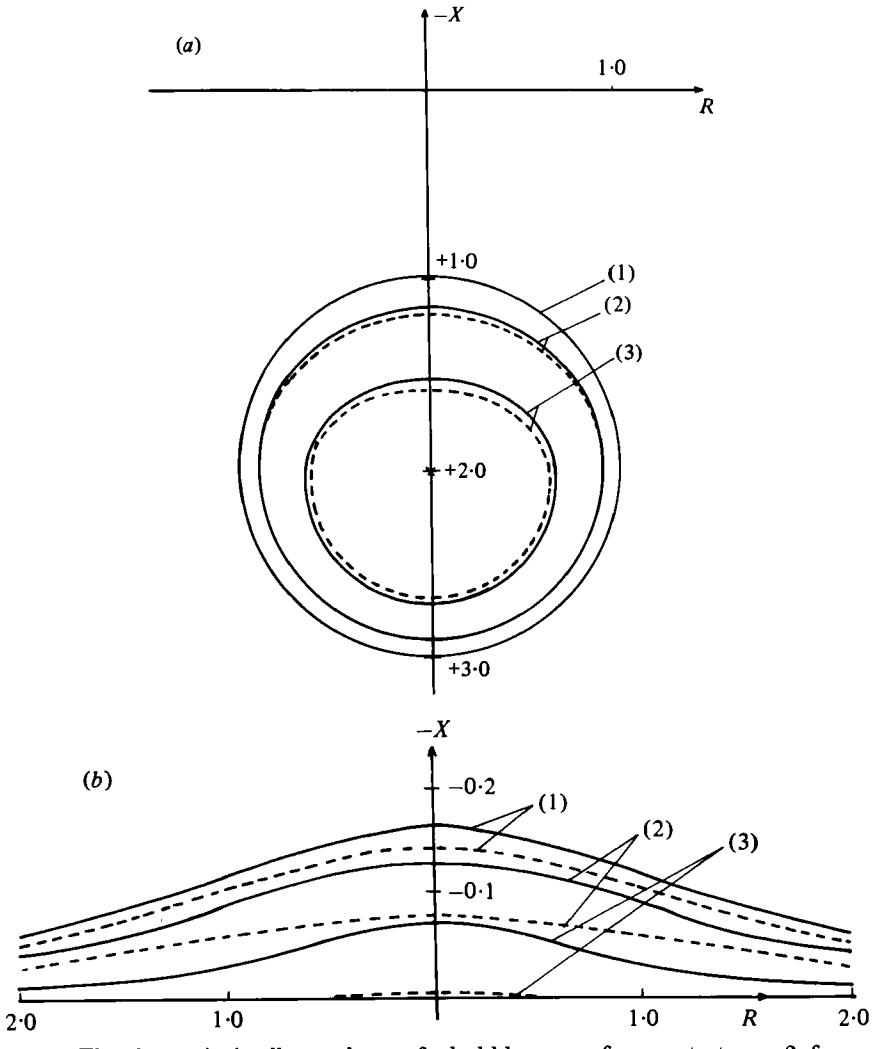

FIGURE 2. (*a*) The theoretical collapse shape of a bubble grown from rest at $\gamma = 2$, for nonlinear (——) and linear (– – –) boundary conditions on the free surface (at dimensionless times (1) 0·78, (2) 1·20, (3) 1·48). (*b*) Theoretical free-surface shape during the collapse of a bubble for nonlinear (——) and linear (– – –) theories, as in (*a*) (at dimensionless times (1) 0·78, (2) 1·20, (3) 1·48). Note 5 times magnification of vertical scale.

This is clearly apparent by the continued motion of the free surface. The effect becomes more pronounced the closer the bubble is brought to the free surface. Illustrations of this will be presented later.

In carrying out the computations it was more convenient to specify the problem in terms of dimensionless variables. Following Gibson & Blake (1980), linear dimensions are made dimensionless with respect to maximum bubble size R_m. Thus the axial co-ordinate x and radial co-ordinate r, together with the initial distance between the vapour bubble centroid and the free surface h, on being made dimensionless now become

$$X = x/R_m, \quad R = r/R_m, \quad \gamma = h/R_m. \tag{22}$$

In the above and following notation, capitals imply dimensionless variables except γ which specifies the initial location of the bubble centroid. A characteristic collapse velocity is $((p_\infty - p_c)/\rho)^{\frac{1}{2}}$, which allows the definition of a time unit and hence a dimensionless time T as follows,

$$t^* = R_m \left[\frac{p_\infty - p_c}{\rho}\right]^{-\frac{1}{2}}, \quad T = t/t^*. \tag{23}$$

It is also convenient to scale the pressure such that it is zero inside the cavity and one at infinity by the following rearrangement,

$$P = (p - p_c)/(p_\infty - p_c). \tag{24}$$

In § 4, theoretical and experimental results will be compared. In the remainder of this section we shall compare the linear and nonlinear theories at $\gamma = 2{\cdot}0$ which according to Chahine (1977) is at the very limit of the validity of linearized boundary conditions on the free surface. In the calculations, the dimensionless time increment ΔT is varied, depending on the change in potential on the bubble surface. Typically it varies from 10^{-4} when the bubble is small and growing rapidly through to $2{\cdot}5 \times 10^{-2}$ when the bubble is near maximum size. Illustrations of the impulse and energy calculations will also be discussed along with the potential deficit at maximum bubble growth.

In figure 2(*a*), the theoretical growth and collapse phases of a vapour bubble, initially at $\gamma = 2{\cdot}0$, for the linear and nonlinear theories are compared for dimensionless times $T = 0{\cdot}78$, $1{\cdot}20$ and $1{\cdot}48$. The shapes of the bubble from both theories are almost identical during the growth phase (1), but during the collapse phase the linear theory is slightly faster (2–3) than the nonlinear model. However, if we calculate the shape of the free surface in the linear theory from the boundary condition

$$\frac{\partial \zeta}{\partial t} = \left[\frac{\partial \phi}{\partial x}\right]_{x=0}, \tag{25}$$

$$\zeta(t + \Delta t) = \zeta(t) + \frac{\partial \zeta}{\partial t}\Delta t + O(\Delta t^2), \tag{26}$$

and compare this value with the nonlinear predictions, a marked difference between their behaviour occurs. These differences are illustrated in figure 2(*b*). During the growth phase of the bubble the free-surface-shape predictions are relatively similar for both theories (note that the vertical scale is magnified by 5); however, during the collapse phase there is a profound difference in the shapes. When the bubble begins to collapse, the linear theory demands that the free surface must also collapse corresponding to a change from a source to a sink behaviour of the bubble. Tbis is not the case for the nonlinear boundary condition, in which case the surface develops a marked hump near the axis of symmetry (3). It will be seen in § 4 that, for smaller values of γ, the free surface continues to extend along the axis of symmetry developing into a pronounced spike.

Evaluation of (20) and (21) yields the kinetic and potential energies respectively. These components are plotted as functions of the dimensionless time T in figure 3(*a*). Initially the total energy is entirely kinetic energy but as the bubble grows there is a gradual change to potential energy reaching a maximum when the bubble is largest, which corresponds approximately to the half-life time of the bubble. The interesting

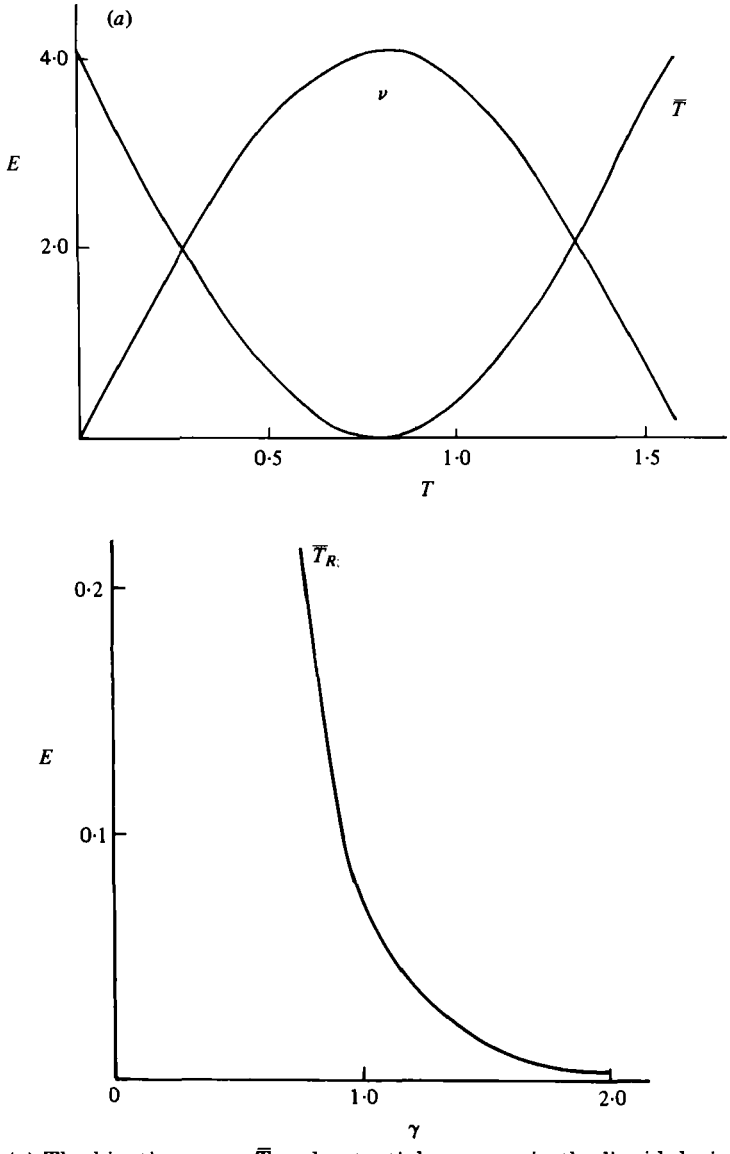

FIGURE 3. (*a*) The kinetic energy $\bar{T}$ and potential energy ν in the liquid during the theoretical growth and collapse of a bubble generated at $\gamma = 2$. (*b*) The effect of free-surface proximity on the residual kinetic energy $\bar{T}_R$ in the liquid when the bubble has reached maximum volume. Note that the total energy in the fluid is approximately $E_0 = 4{\cdot}2$.

feature of this free-surface case is that at maximum bubble size there exists a residual kinetic energy $\bar{T}_R$ in the fluid, its magnitude depending on the initial location of the bubble, γ. This is illustrated in figure 3(*b*), where we can observe a steep rise in the residual kinetic energy $\bar{T}_R$ as γ decreases.

In figure 4, the Kelvin impulse as calculated by evaluation over the bubble surface $\mathbf{I}_0$ (in equation (17) we actually need only evaluate the x-component) is compared against the evaluation over the free surface $\mathbf{I}_1$ (18). It is easier to illustrate the variation between $\mathbf{I}_0$ and $\mathbf{I}_1$ by plotting the difference $\epsilon = \mathbf{I}_0 - \mathbf{I}_1$ as a function of the dimen-

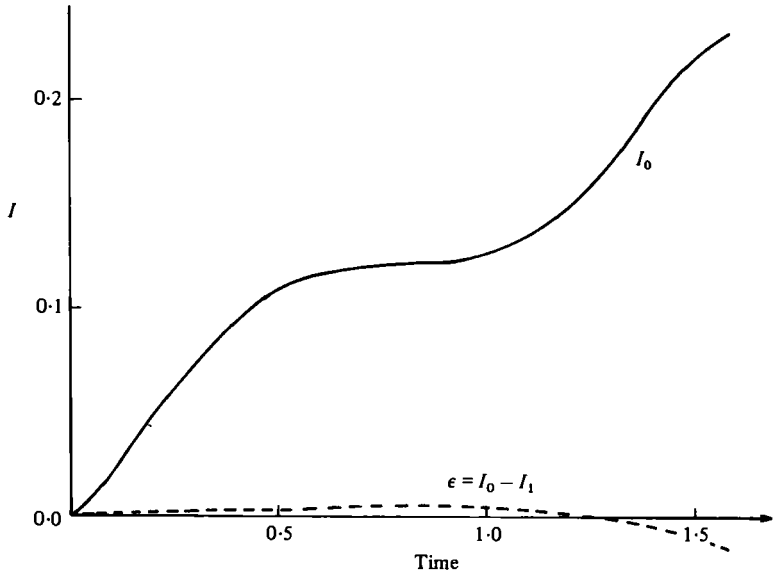

FIGURE 4. Calculations of Kelvin impulse on the bubble surface and the free surface ($\gamma = 2$).

sionless time T. The sign of the impulse is positive, in contrast to a rigid boundary which has a negative sign; further discussions on the importance of the impulse can be found in Blake & Cerone (1981). Near the half-life time the impulse curve is flat, corresponding to a zero growth rate (i.e. zero source strength) of the bubble. At large times ($T > 1{\cdot}5$) ϵ begins to increase rapidly, so the calculation is terminated.

Further examples of these calculations are shown in § 4 where the predicted behaviour is compared against observation; the details of the experiments and apparatus being described in the next section.

3. Experimental apparatus and techniques

The apparatus used in these experiments is similar to that of Benjamin & Ellis (1966) and Gibson (1972). The central part is a 370 mm deep, 260 mm internal diameter, Perspex tank, filled with distilled water to a height of 213 mm. The water is degassed by evacuating the tank and shaking it vigorously in a vertical direction for about half an hour. A high-voltage spark probe, that can be traversed along the centreline, extends into the tank from the floor. A 25 mm fine wire square measurement scale is attached to the probe beneath the spark gap. The scale, the probe and the water surface are viewed through a flat 25 mm thick Perspex window recessed into the sidewall of the tank.

The tank is mounted on a horizontal platform suspended between vertical guide rails by an electromagnet. A HYCAM high-speed ciné camera, fitted with a half-frame 16 mm prism, and a PAL, 2·4 kW, continuous light source are also mounted on the platform. The vapour bubble is generated by an electric spark discharged from a 0·25 μF condenser at 8500 V. The bubble is illuminated from behind by the light source and photographed at a rate of approximately 11 000 frames s^{-1} by the ciné camera.

Water temperature (°C)	Tank pressure (kPa)	Spark gap depth h (mm)	Maximum bubble radius R_m (mm)
18·5	6·93	40	17·5
17·3	6·93	30	17·9
17·3	6·93	20	17·2
18·3	6·67	20	20·3
18·5	6 93	10	17·9
18·0	6·67	10	20·5

TABLE 1. Experimental conditions for vapour-bubble experiments

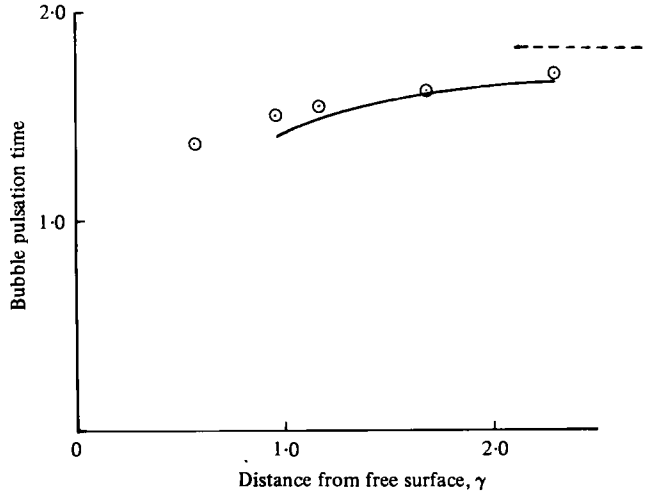

FIGURE 5. The effect of a free surface on vapour-bubble pulsation time (——, theory; ⊙, experiment; – – –, infinite liquid limit).

In order to study relatively large, slowly pulsating bubbles without buoyancy affecting their motion, the experiments are performed with the tank in free fall. Each experiment follows a similar pattern. The spark probe is set at a prescribed depth h beneath the free surface, the tank pressure is reduced to about 7 kPa, and the camera set in motion. When the camera accelerates to the desired framing rate it triggers the spark and releases the electromagnet. The platform then falls from a state of rest while the bubble grows and collapses, and the camera records its motion. After development the film negative is analysed on a standard microfiche reader with a 24:1 magnification.

4. Results and discussion

Our numerical model of the bubble and free-surface motion, with the nonlinear free-surface boundary condition has been compared with experimental bubbles generated under the conditions shown in table 1.

For the purpose of comparison, p_c was equated with the saturation vapour pressure of water, p_∞ was equated with the tank pressure above the water and R_m was equated with half the maximum horizontal width of the experimental bubble.

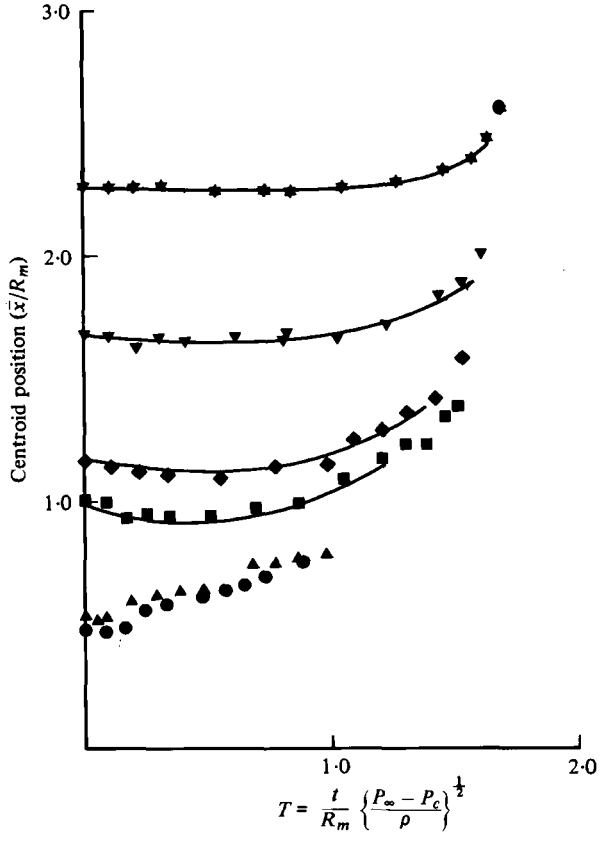

FIGURE 6. Motion of bubble centroid during growth and collapse of a vapour bubble near a free surface. ——, theory; experiment: ●, $\gamma = 0{\cdot}49$; ▲, $\gamma = 0{\cdot}56$; ■, $\gamma = 0{\cdot}98$; ◆, $\gamma = 1{\cdot}17$; ▼, $\gamma = 1{\cdot}68$; ★, $\gamma = 2{\cdot}26$.

Figure 5 compares theoretical estimates and experimental measurements of the bubble pulsation time as a function of initial distance from the free surface. There is good agreement down to $\gamma = 1$, at which stage the numerical model becomes inaccurate relatively early in the collapse. Figure 6 shows the centroid motion of the six experimental bubbles and theoretical estimates of the first four described in table 1. Again agreement between theory and experiment is satisfactory. The key features are that the slight early motion towards the free surface during the expansion is completely outweighed by subsequent movement away during the collapse.

Figures 7 and 8 compare theoretical and experimental bubble and free-surface interactions for $\gamma = 1{\cdot}68$ and $0{\cdot}98$ respectively. It is not possible to compare the bubble shapes at exactly the same time because of the different discrete time increments used in theory and experiment. In the first case ($\gamma = 1{\cdot}68$) the bubble remains remarkably spherical throughout the expansion and there is only a small hump formed on the free surface. During the collapse, downward migration of the centroid is clearly evident, the free surface subsides and the bubble becomes involuted from above; the theoretical model breaks down at the time that the jet is about to form in the bubble. In the second case ($\gamma = 0{\cdot}98$) the bubble becomes elongated along the axis of

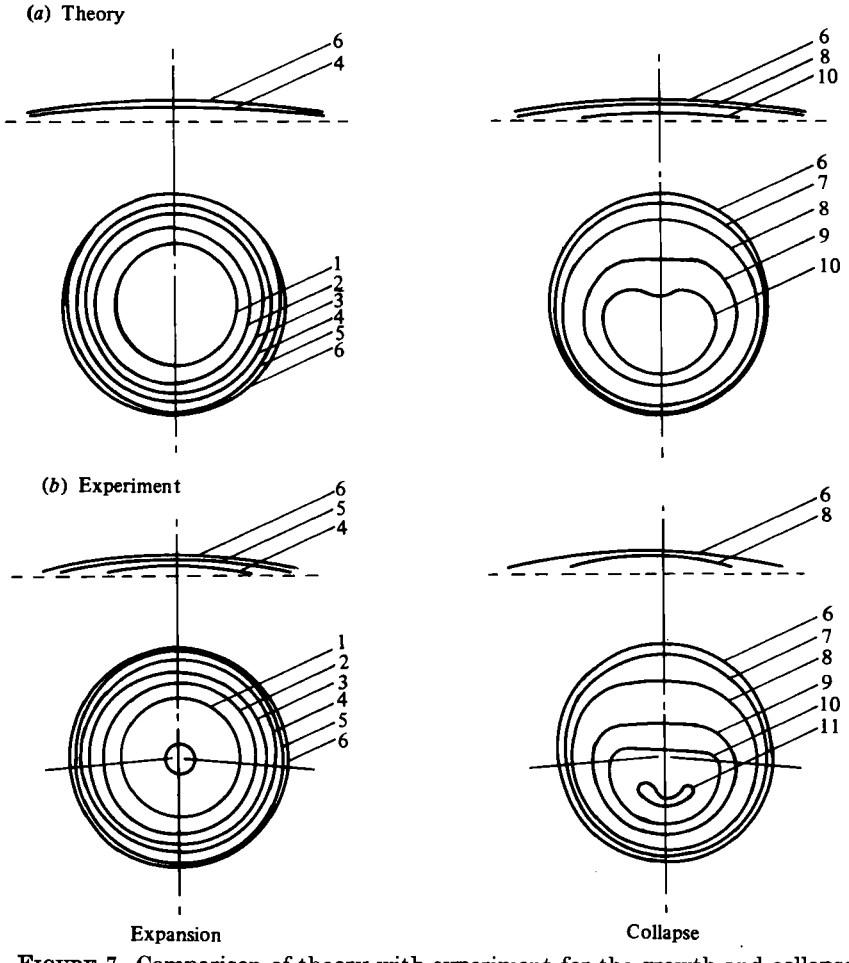

FIGURE 7. Comparison of theory with experiment for the growth and collapse of a vapour bubble near a free surface ($\gamma = 1{\cdot}68$).

Contour no. ...	1	2	3	4	5	6	7	8	9	10	11
Time (theory)	0·107	0·198	0·298	0·398	0·623	0·823	1·023	1·223	1·432	1·539	—
Time (exp't)	0·102	0·205	0·307	0·410	0·615	0·820	1·025	1·230	1·434	1·537	1·609

symmetry during the expansion and causes a substantial free-surface hump. During the collapse the hump evolves into a sharp spike that continues to advance along the axis of symmetry, while contracting in width at the base. Thus, on the axis of symmetry, during the collapse, theory predicts and experiment shows that the free surface and the adjacent bubble-surface motions are completely out of phase.

When making this comparison a small, but consistent, difference was observed between theoretical and experimental free-surface shapes. This proved to be an optical illusion caused by the different refractive indices of the gas and liquid in the tank. The free-surface image is contracted linearly by about 3 % in comparison to the bubble image.

A striking free-surface bubble interaction is shown clearly in figure 9 and figure 10. In this case the bubble was generated at a value of $\gamma = 0{\cdot}56$. The theoretical model

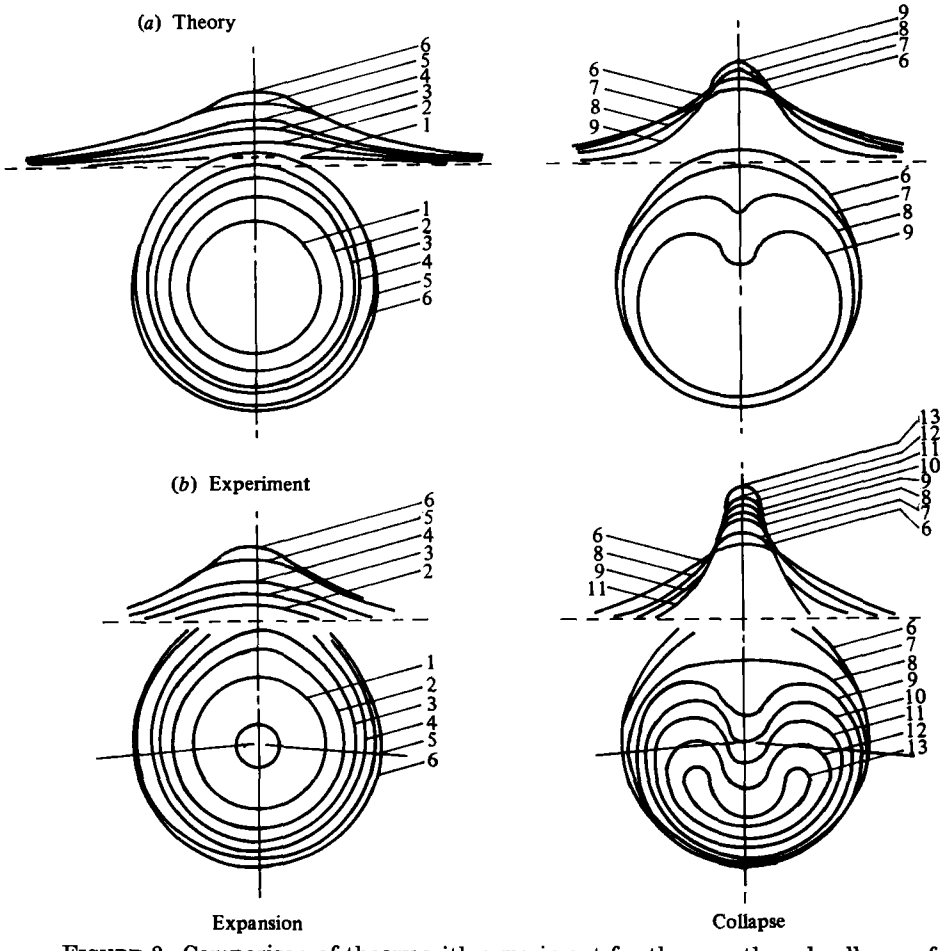

FIGURE 8. Comparison of theory with experiment for the growth and collapse of a vapour bubble near a free surface ($\gamma = 0{\cdot}98$).

Contour no. ...	1	2	3	4	5	6	7	8	9	10	11	12	13
Time (theory)	0·088	0·172	0·263	0·338	0·513	0·688	0·863	1·037	1·212	—	—	—	—
Time (exp't)	0·087	0·173	0·260	0·347	0·520	0·604	0·867	1·040	1·214	1·300	1·387	1·474	1·508

breaks down early in the bubble expansion phase, but our experiment shows the free-surface spike developing before the expansion concludes, and continuing to grow to quite long and slender proportions in the ensuing bubble collapse. It also shows that the bubble is entrained well into the base of the elevated free surface during the expansion and then becomes involuted by the formation of a very slender jet that moves with great speed down the axis of symmetry in the opposite direction to the growing free-surface spike. The jet is disrupted when it strikes the spark probes, but it clearly reaches the lower side of the bubble before the collapse is complete. The free-surface spike persists throughout the subsequent bubble pulsations, gradually becoming narrower. The last frame in figure 10 shows the spike when the torus formed by involution of the bubble has reached its minimum size.

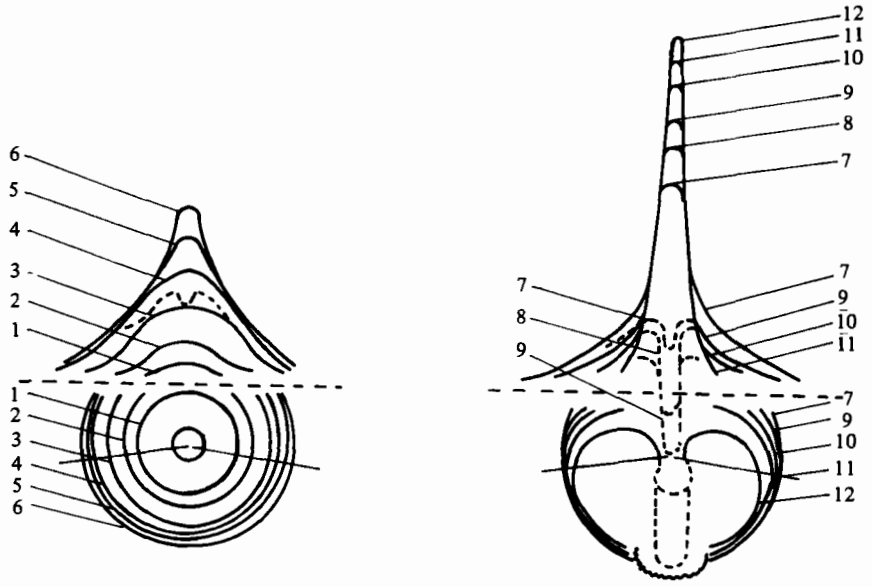

FIGURE 9. Experimental growth and collapse of a vapour bubble near a free surface ($\gamma = 0.56$).

Contour no. ...	1	2	3	4	5	6	7	8	9	10	11	12
Time (exp't)	0·048	0·087	0·194	0·291	0·387	0·484	0·581	0·678	0·775	0·872	0·969	1·066

5. Conclusions

The approximate integral-equation approach developed here is adequate to describe the growth and collapse of a vapour bubble generated at least one maximum radius from the free surface. Correct prediction of the bubble and free-surface distortion can only be achieved when the complete nonlinear Bernoulli pressure condition is applied at the free surface and the bubble surface. It is therefore probable that calculations of vapour bubble and flexible boundary interactions will require similar precision.

In the absence of buoyancy effects a vapour bubble may be generated within half a maximum radius of the free surface without venting. At its maximum size much of the bubble is entrained beneath the elevated free surface, but still a liquid jet forms and penetrates the bubble from above. The distortion of the adjacent deformable boundary during bubble expansion is significant. It is therefore essential to consider the expansion when seeking to describe bubble/flexible-boundary interaction during the collapse.

We wish to acknowledge the contribution of our photographer, Mr Neil Hamilton, whose efforts were essential to capture the beauty of this phenomenon.

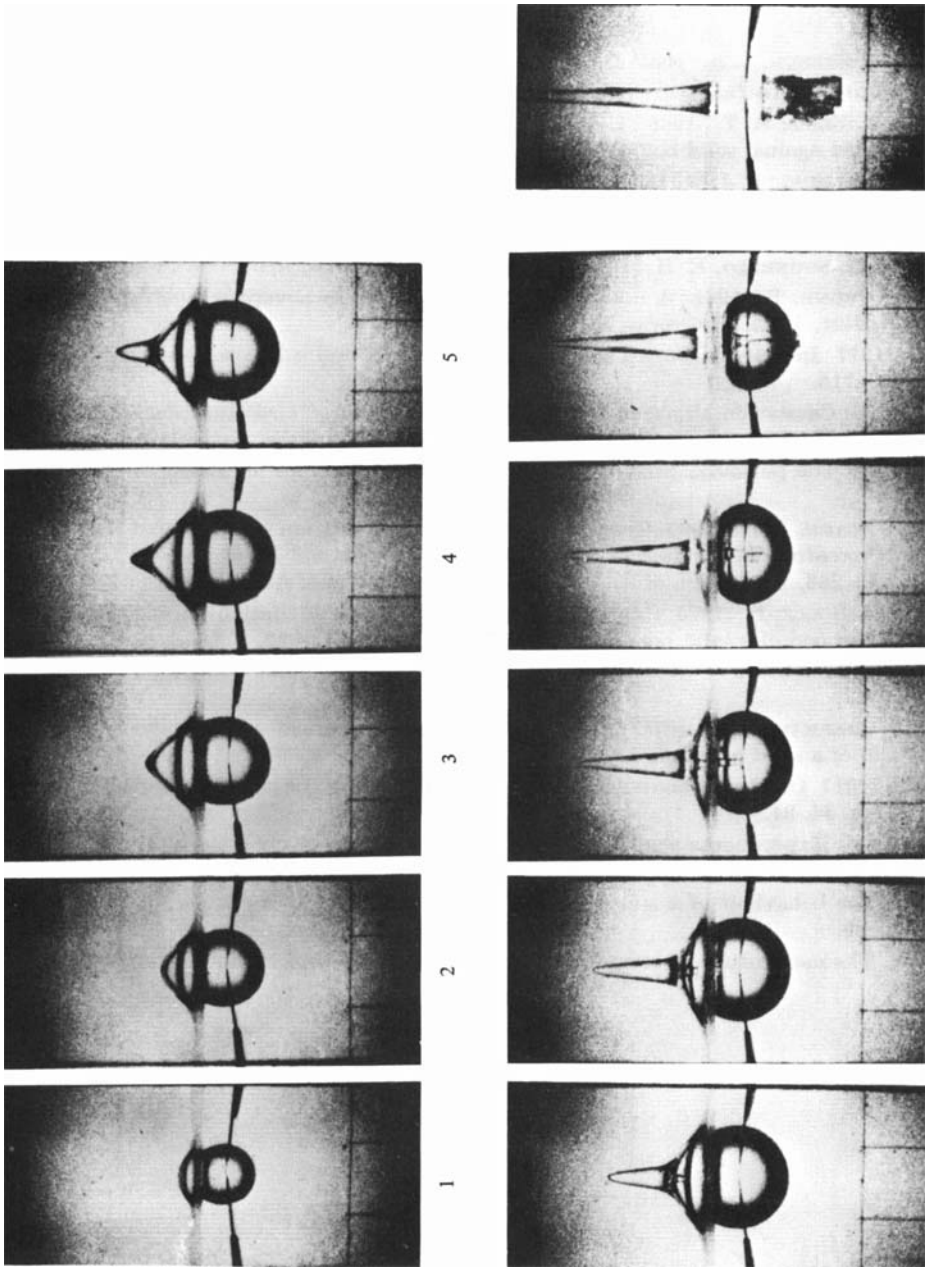

FIGURE 10. Growth and collapse of a vapour bubble close to a free surface. Water temperature = 18·5 °C, p_∞ = 6·93 kPa, R_m = 17·9 mm. [Time from spark discharge (ms): (1) 0·8, (2) 1·6, (3) 2·4, (4) 3·2, (5) 4·0, (6) 4·7, (7) 5·5, (8) 6·3, (9) 7·1, (10) 7·9, (11) 11·2.]

REFERENCES

ABRAMOWITZ, M. & STEGUN, I. A. 1965 *Handbook of Mathematical Functions*. Dover.

BATCHELOR, G. K. 1967 *An Introduction to Fluid Dynamics*. Cambridge University Press.

BENJAMIN, T. B. & ELLIS, A. T. 1966 The collapse of cavitation bubbles and the pressures thereby produced against solid boundaries. *Phil. Trans. Roy. Soc.* A **260**, 221.

BEVIR, M. K. & FIELDING, P. J. 1974 Numerical solution of incompressible bubble collapse with jetting. In *Moving Boundary Problems in Heat Flow and Diffusion* (ed. J. R. Ockendon & W. R. Hodgkins). Clarendon Press.

BIRKHOFF, G. & ZARANTONELLO, E. H. 1957 *Jets, Wakes and Cavities*. Academic Press.

BLAKE, J. R. & CERONE, P. 1981 A note on the 'impulse' due to a vapour bubble near a boundary. *J. Aust. Math. Soc.*, series B (in press).

CHAHINE, G. L. 1977 Interaction between an oscillating bubble and a free surface. *J. Fluids Engng* **99**, 709–716.

GIBSON, D. C. 1968 Cavitation adjacent to plane boundaries. *Proc. Third Australasian Conf. on Hydraulics & Fluid Mechanics*, pp. 210–214. Institution of Engineers, Sydney, Australia.

GIBSON, D. C. 1972 The pulsation time of spark induced vapor bubbles. *J. Basic Engng* **94**, 248–249.

GIBSON, D. C. & BLAKE, J. R. 1980 Growth and collapse of cavitation bubbles near flexible boundaries. *Proceedings of the Seventh Australasian Hydraulics and Fluid Mechanics Conference*, pp. 283–286. Institution of Engineers, Australia, Brisbane, August 1980.

LAUTERBORN, W. & BOLLE, H. 1975 Experimental investigations of cavitation-bubble collapse in the neighbourhood of a solid boundary. *J. Fluid Mech.* **72**, 391–399.

MITCHELL, T. M. & HAMMITT, F. G. 1973 Asymmetric cavitation bubble collapse. *J. Fluids Engng* **95**, 29–37.

PLESSET, M. S. & CHAPMAN, R. B. 1971 Collapse of an initially spherical vapour cavity in the neighbourhood of a solid boundary. *J. Fluid Mech.* **47**, 283.

RAYLEIGH, LORD 1917 On the pressure developed in a liquid during the collapse of a spherical void. *Phil. Mag.* **34**, 94.

REYNOLDS, O. 1894 Experiments showing the boiling of water in an open tube at ordinary temperatures. *British Assoc. Adv. Sci. Report* 564. (See also *Science Papers* **2**, p. 578, 1901.)

SHIMA, A. 1968 The behaviour of a spherical bubble in the vicinity of a solid wall. *J. Basic Engng* **90**, 75–89.

WU, T. Y. 1976 The momentum theorem for a deformable body in perfect fluid. *Schiffstechnik* **23**, 229–232.